A bimetallic sulfide Co_9S_8/MoS_2/C heterojunction in a three-dimensional carbon structure for increasing sodium ion storage

CHEN Hong, MU Jian-jia, BIAN Yu-hua, GAO Xuan-wen*,
WANG Da, LIU Zhao-meng, LUO Wen-bin*

（*Institute for Energy Electrochemistry and Urban Mines Metallurgy*, *School of Metallurgy*, *Northeastern University*, *Shenyang* 110819, *China*）

Abstract: The synthesis of high-rate and long-life anode materials for sodium ion batteries (SIBs) has attracted much attention. However, the slow kinetics and large increase in volume of the batteries remain major problems. Both metal-organic frameworks and MoS_2 have shown properties suitable for SIBs, making research on their composite systems an attractive area of research. We report the formation of flower-like Co_9S_8/MoS_2/C composites by a simultaneous vulcanization-carbonization process using $MoCl_5$ as the Mo source and a 2-methylimidazole cobalt salt as the Co and C precursor at different temperatures（600, 700 and 800 °C）in sublimed sulfur. The effect of the heterojunction on the diffusion kinetics was analyzed using density functional theory. The results indicate that the electronic structure is different at the interface in the heterogeneous structure, exhibiting typical metallic properties and better electronic conductivity. In addition, the anode material Co_9S_8/MoS_2/C synthesized at 700 °C had the most stable structure and best electrochemical performance of the three samples. Notably, the discharge capacity of Co_9S_8/MoS_2/C-700 fully recovered from 368 to 571 mAh g^{-1} and then stabilized at 543 mAh g^{-1} when the current density was restored from 4 000 to 40 mA g^{-1}. This work demonstrates the preparation of heterojunction materials for composite anode materials as a step to producing high-performance metal SIBs.

Key words: Sodium ion batteries; Anode; Metal-organic frame; MoS_2; Co_9S_8

1 Introduction

Lithium-ion batteries are now commonly employed in portable consumer electronics gadgets as well as emerging electric vehicles[1–2]. However, the massive rise of lithium-ion batteries (LIBs) implies a jump in lithium resource prices, as well as a limited and uneven distribution of lithium reserves around the globe, limiting the development of LIBs[3–5]. Due to their abundant materials and similarity with lithium's chemistry, sodium-ion batteries (SIBs) have drawn a great deal of interest and are considered capable of partially replacing LIBs[6–7]. Transition metal sulfides (TMS) have received a great deal of attention as anode materials for SIBs due to their enormous theoretical capacity and high safety, as well as their higher electrical conductivity and faster charge-discharge reaction kinetics than oxides. Among recently produced anode materials, MoS_2 is a classic example of TMS, with simple preparation, abundant raw materials, high interlayer spacing (0.62 nm) and weak interlayer van der Waals forces[8–11]. TMS does, however, have several flaws. On one hand, TMS experiences severe volume expansion during charge and discharge, causing cycle stability to be poor[12]. On the other hand, although than oxides, TMS have generally lower conductivity which causes delayed electrochemical reaction kinetics and results in inadequate rate performance[13–14].

The construction of heterogeneous metal sulfides is an effective method for addressing the drawback of low electrical conductivity[15–16]. When compared to single-phase metal sulfides, heterogeneous metal sulfides can not only promote the creation of an internal electric field, but also enhance the activity of electrochemical reactions at the heterointerface, in-

Received date: 2023-01-05; **Revised date:** 2023-02-28

Corresponding author: GAO Xuan-wen, Associate Professor. E-mail: gaoxuanwen@mail.neu.edu.cn;
LUO Wen-Bin, Professor. E-mail: luowenbin@smm.neu.edu.cn

Author introduction: CHEN Hong, Ph.D candidate. E-mail: 2010750@stu.neu.edu.cn

Supplementary data associated with this article can be found in the online version.

creasing electrical conductivity[17–19]. It can also improve crystallinity at the heterointerface, as well as induce lattice mismatches, distortions and defects, allowing the reaction kinetics of electrode materials to be tuned[20–22]. Due to the continuous insertion and conversion/alloying reaction in SIBs, there is rapid volume change of electrode materials. To solve the above problems, porous nanostructure engineering can be constructed to improve the stability of sodium storage performance of mixed metal sulfides.

Metal-organic frameworks (MOFs), as porous inorganic-organic hybrid materials with high specific surface area, controllable structure, and tunable pore size, are widely used as precursors for the preparation of carbon-metal or metal sulfide composites[23–25]. In general, MOFs exhibit impressive performance as active materials for energy storage due to their complex and varied structural advantages[26–28]. Moreover, the nanostructure of MOFs can not only shorten the diffusion path of Na ions, but also withstand the volume expansion caused by the insertion of Na ions, providing a stable support for the overall structure[28–29].

With the aim of overcoming the weaknesses of any single component, in this work, a flower-like Co_9S_8/MoS_2/C composite was designed and constructed by a simultaneous vulcanization-carbonization method at different temperatures using Co-ZIF as precursor and adding Mo source. By systematically investigating the effect of sulfur vacancies and microtopography on sodium storage behaviour, the flower-like Co_9S_8/MoS_2/C microspheres formed by interconnected nanosheet arrays (Co_9S_8/MoS_2/C-700) possess the best electrochemical performance. Heterogeneous metal sulfides can not only enhance the electrical conductivity of the electrode material due to the heterostructure, but also facilitate electron/ion transport. Most importantly, the spherical structure provides a stable support and the porous structure provides a buffer space for the volume deformation caused by subsequent redox reactions. It is worth noting that the discharge capacity of Co_9S_8/MoS_2/C-700 can fully recover from 368 to 571 mAh g^{-1} and then stabilize at 543 mAh g^{-1} when the current density is restored from 4 000 to 40 mA g^{-1}.

2 Experimental

2.1 Materials synthesis

ZIF-67 was synthesized by a room temperature precipitation method that has been reported previously[30]. Typically, $Co(NO_3)_2·6H_2O$ (5.82 g, 0.02 mol) and 2-MeIm (6.16 g, 0.075 mol) were dissolved in 150 mL of methanol to form clarified liquor. Then, the solution of 2-MeIm mixture was poured into the solution of $Co(NO_3)_2·6H_2O$ and stirred evenly at room temperature for 24 h. Finally, the purple ZIF-67 was obtained by centrifuging the mixture and washing several times with methanol and drying at 60 °C overnight.

20 mg of the above ZIF-67 template was dispersed in 40 mL CH_3OH to form a uniform solution. Then 1.5 mL $MoCl_5$ (0.2 mol L^{-1}) solution and 0.166 4 g of NH_4HCO_3 were successively added to the suspension. After magnetic stirring for 7 h, the brown precipitate was collected by centrifugation, washed three times with deionised (DI) water, and dried at 60 °C overnight.

Co_9S_8/MoS_2/C-700 was fabricated by a simultaneous vulcanization-carbonization method. 0.02 g of as-prepared Mo-based precursor and 0.05 g of sublimed sulphur were uniformly mixed and placed in the centre of a quartz tube. After rinsing with high-purity argon, the furnace was heated to 700 °C at a heating rate of 5 °C min^{-1} and maintained for 1 h under a H_2/Ar (90% *v*/*v*) mixed atmosphere.

For comparison, the samples of Co_9S_8/MoS_2/C-600 and Co_9S_8/MoS_2/C-800 were also synthesized in the same manner under the same conditions except the calcination temperature was 600 °C and 800 °C, respectively.

2.2 Materials characterization

The phase compositions of the ZIF-67 template and Co_9S_8/MoS_2/C-700, 600, 800 were analysed by X-ray diffraction (XRD) (Deutschland BRUKER D8) using Cu-*Kα* radiation. Scanning electron microscopy (SEM SU8220, Hitachi High-Tech Company), high-resolution transmission electron microscopy (HRTEM)

and a super-X EDS detector system (Bruker, Super-X, USA) was used to examine the morphology, microstructure of the samples and energy dispersive spectrometry (EDS) elemental maps. X-ray photoelectron spectroscopy (XPS, Thermo ESCALAB 250XI Al *K*α X-ray source) were used to analyze elemental chemical compositions of material.

2.3 Electrochemical measurements

The as-obtained active material, carbon black, and sodium carboxymethyl cellulose (CMC) were mixed with DI water in a weight ratio of 7∶2∶1 to form a slurry, and coated on Cu foil. The coated foil was dried at 80 °C in vacuum overnight and cut into discs with a diameter of 12 mm. Glass fiber was used as the separator and metallic sodium was used as counter electrode for SIBs. 1.0 mol L^{-1} $NaClO_4$ dissolved in EC/DMC (1∶1, volume ratio) with FEC (5%, mass fraction) was used as electrolyte. The above working electrode, glass fiber, electrolyte and counter electrodes were assembled in a glove box of Ar atmosphere to obtain the half-cells. The charge and discharge test measurement was carried out in the voltage range of 3.0-0.01 V versus Na/Na^+ at room temperature (25 °C) using LAND CT2001A testing system. Cyclic voltammetry (CV) tests were conducted on an LANHE M340A instrument electrochemical workstation between 0.01 and 3.0 V *vs*. Na^+/Na with the stated scan rates. Electrochemical impedance spectroscopy (EIS) was carried out on the Princeton 2273 at frequencies of 100 kHz to 10 MHz.

2.4 Density functional theory calculation

The density functional theory (DFT) calculations were performed using the Vienna Ab initio Simulation Package (VASP)[31–32]. The Perdew-Burke-Ernzerhof (PBE) functional generalized gradient approximation (GGA) was considered to describe the exchange-correlation. The kinetic energy cutoff for the plane wave was about 520 eV, which was applied for the wave function expansion of S, Mo and Co. In addition, Brillouin zone integration on the grid with a 3 × 3× 3 and 12 ×12 × 1 k grid mesh was carried out to achieve geometry optimization and calculation of the density of states (DOS), respectively. The Mo and Co atoms use the DFT+U technique, where the U–J parameters for Mo and Co states are set to be 5.5 and 3.32 eV, respectively. The quasi-Newton method with energy and force convergence criteria, and the Newton method with energy and force convergence criteria of 1.0×10^{-6} eV per atom and 0.01 eV $Å^{-1}$ in the structural optimization were performed for MoS_2 and Co_9S_8 to obtain high accuracy. The van der Waals interaction force was analyzed with a semi-empirical DFT-D3 method. Virtual interaction was avoided by applying a 15 Å vacuum layer thickness.

3 Results and discussion

3.1 Structure and composition

The synthesis process of the flower-like $Co_9S_8/MoS_2/C$ nanocomposite is schematically illustrated in Fig. 1a. The uniform ZIF-67 nanocrystal precursor was generated by a solvothermal technique, as evidenced by scanning electron microscopy (SEM) image (Fig. S1a). Then, molybdenum pentachloride was added to the solution containing ZIF-67 precursor as a molybdenum source to obtain a uniform molybdenum precursor. Finally, because the electronegativity of Co (1.9) is slightly higher than that of Mo (1.8), Co and Mo ions will react with sulfur powder at high temperature to form Co_9S_8, and then cause the heterogeneous nucleation and subsequent growth of MoS_2 nanoparticles on the surface of Co_9S_8.

The crystal structure of as-synthesized sample was studied by X-ray diffraction (XRD). The XRD pattern of the $Co_9S_8/MoS_2/C$ composite prepared at different temperatures (600, 700, 800 °C) are shown in Fig. 1b. As expected, all samples show similar diffraction patterns. There are a series of diffraction peaks around 14.1°, 32.5°, 58.1° and 60.1°, which should be indexed to the (002), (101), (103), (110) and (008) planes of the MoS_2 (JCPDS No.75-1539). And other peaks at 29.6° and 51.2° can also be observed, which match well with the (311) and (440) planes of cubic Co_9S_8 (JCPDS No. 86-2273). These prove the formation of the MoS_2 and Co_9S_8 phases in the polyhedral structures. Additionally, there is no diffraction peak of S in the image. The XRD results show the high purity of the synthesized sample.

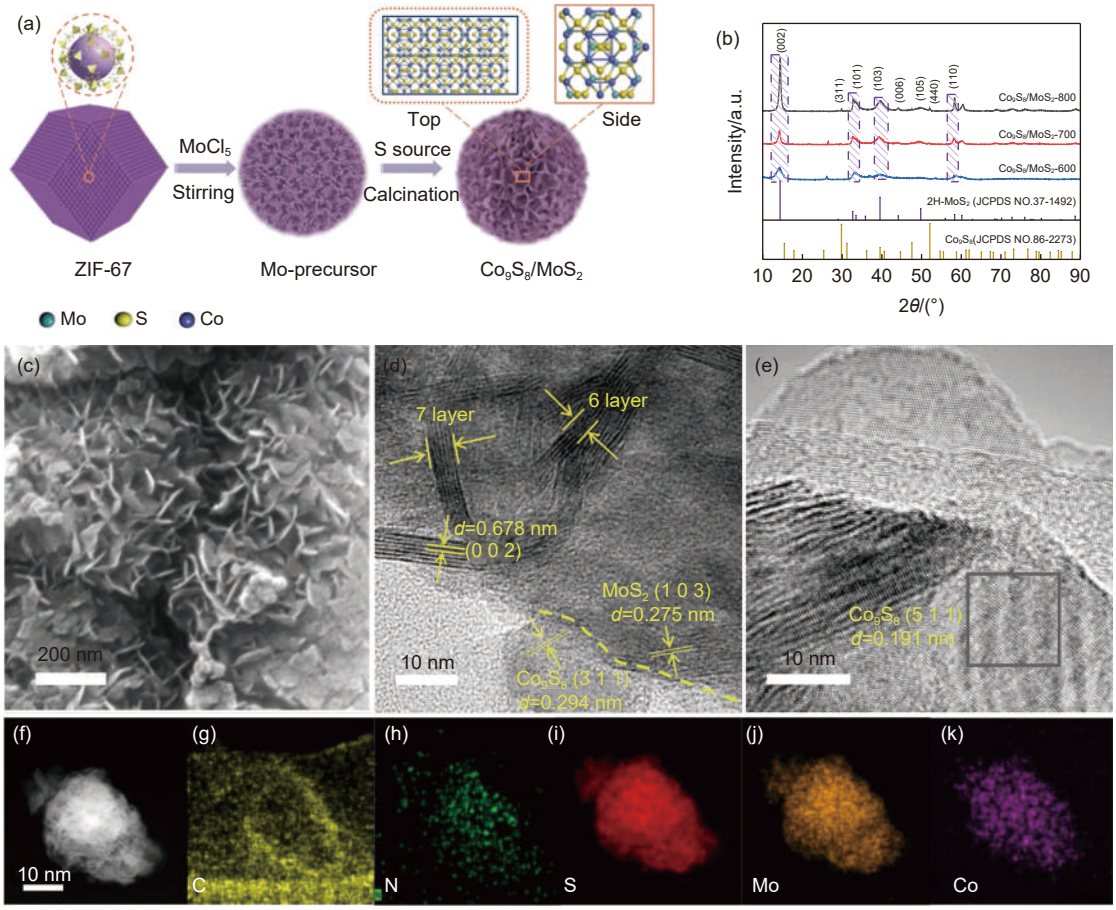

Fig. 1　(a) Schematic illustration of the flower-like Co_9S_8/MoS_2/C heteroball. (b) XRD patterns ZIF-67 precursor and Co_9S_8/MoS_2/C synthesized at 600 °C, 700 °C, 800 °C. (c) SEM image and (d, e) HRTEM image of Co_9S_8/MoS_2/C-700. (f-k) EDS mapping images of the flower-like Co_9S_8/MoS_2/C-700 hetero-ball

SEM and TEM were used to investigate the morphology and microstructure of the material. It can be clearly seen from Fig. S1a that the ZIF-67 precursor is a regular polyhedron. In addition, the prepared ZIF-67 is a uniform polyhedron of similar size as shown in Fig. S1b. In Fig. S1c-d and Fig. 1c, the smooth surface of ZIF-67 is completely covered by a large number of folds, which are composed of vertical and cross-linked arrays of MoS_2 nanosheets. To increase the degree of crystallinity in the product, the calcination temperature is 600-800 °C. In addition, these prepared nanosheets are also connected to each other, providing abundant open spaces and active sites, forming a typical loose and porous architectural structure. As can be seen from Fig. S2, with the gradual increase of temperature, the crystallinity of the material increases and there is partial collapse on the sur face. When the temperature was increased to 800 °C, the degree of crystallization increased and the shape of the resulting Co_9S_8/MoS_2/C-800 microspheres was distorted, and due to the collapse of the active material at higher temperatures, many nanosheets were irregularly aggregated. This would greatly reduce the probability of ion insertion and extraction. Considering the influence of temperature on crystallinity and electrochemical properties, Co_9S_8/MoS_2-700 could achieve far superior performance than other samples, and will be discussed in the following section. To gain further insight into the composition and microstructure of the Co_9S_8/MoS_2/C-700, the element mapping spectra and TEM analyses were performed. The TEM image (Fig. 1d-e) revealed the intimate contact between MoS_2 nanoparticles and the Co_9S_8 substrate. The abundant hetero-interface created may act as active sites for fast Na^+ storage[33]. Fig. 1d shows MoS_2 nanosheets with approximately 7 atomic layers formed on a porous skeleton substrate. In Fig. S3(a-b), the lattice spacing of MoS_2 and were 0.678 nm

(002) and 0.275 nm (103), and Fig. S3c shows the (311) plane of rutile Co_9S_8 corresponding to the lattice fringe of 0.294 nm. From Fig. 1(f-k), the S, Mo and Co elements are uniformly distributed throughout the whole microsphere.

X-ray photoelectron spectroscopy (XPS) analysis was then conducted to investigate the samples and binding states of each element. Fig. S4a shows the survey spectrum of the Co_9S_8/MoS_2/C-700 hetero-ball. The survey XPS spectrum testifies the existence of C, N, Mo, Co, O and S elements. Fig. S4b depicts the C 1s spectrum fitted into 3 peaks at binding energies of 284.8, 286.4 and 288.8 eV, which should be related to the C—C, C—N/O and C=O bonds, respectively[34]. In the Mo 3d spectrum (Fig. 2a), the two major peaks at 232.0 and 229.1 eV are in good agreement with Mo $3d_{3/2}$ and Mo $3d_{5/2}$ of Mo^{4+}, further confirming the formation of MoS_2 in the simple. The peak at 226.3 is assigned to S 2s[35]. Meanwhile, the two weak peaks located at 236.0 eV are attributed to the Mo^{6+} because of slight surface oxidation[36]. The high-resolution Co 2p spectrum exhibits six main peaks at 778.9, 782.6, 786.9, 794.1, 798.7 and 804.6 eV (Fig. 2b). Among them, the binding energies at 778.9 and 794.1 eV correspond to Co $2p_{3/2}$ and Co $2p_{1/2}$, and the 2 satellite peaks at 804.6 and 786.9 eV can be attributed to the typical peaks for Co^{3+}. Strong peaks at 782.6 and 798.7 eV could be attributed to Co $2p_{3/2}$ and Co $2p_{1/2}$ of Co^{2+}[37].

For the N 1s core-level XPS spectrum of Co_9S_8/MoS_2/C-700 (Fig. 2c), 4 peaks can be fitted, corresponding to Mo 3p (394.9 eV) and 3 different types of N species, where the N species are pyridine (398.7 eV), pyrrole (400.1 eV) and graphite (401.0 eV)[38]. The reason of the sample containing N is that the organic ligand (2-MIM) rich in nitrogen is decomposed in the process of high temperature calcination. It is found that pyridine nitrogen and graphite nitrogen are the dominant species, which can improve the conductivity of ions and electrons[39]. For the spectrum in Fig. 2d, the characteristic peaks are located at 162.0 for S $2p_{3/2}$ and 163.2 eV for S $2p_{1/2}$, indicating that sulphur is present in S^{2-} state in Co_9S_8/MoS_2/C[40]. In addition, one more peak at 169 eV corresponds to a shake-up satellite peak of sulphur (polysulfide or oxidized group)[41]. The presence of O element in the

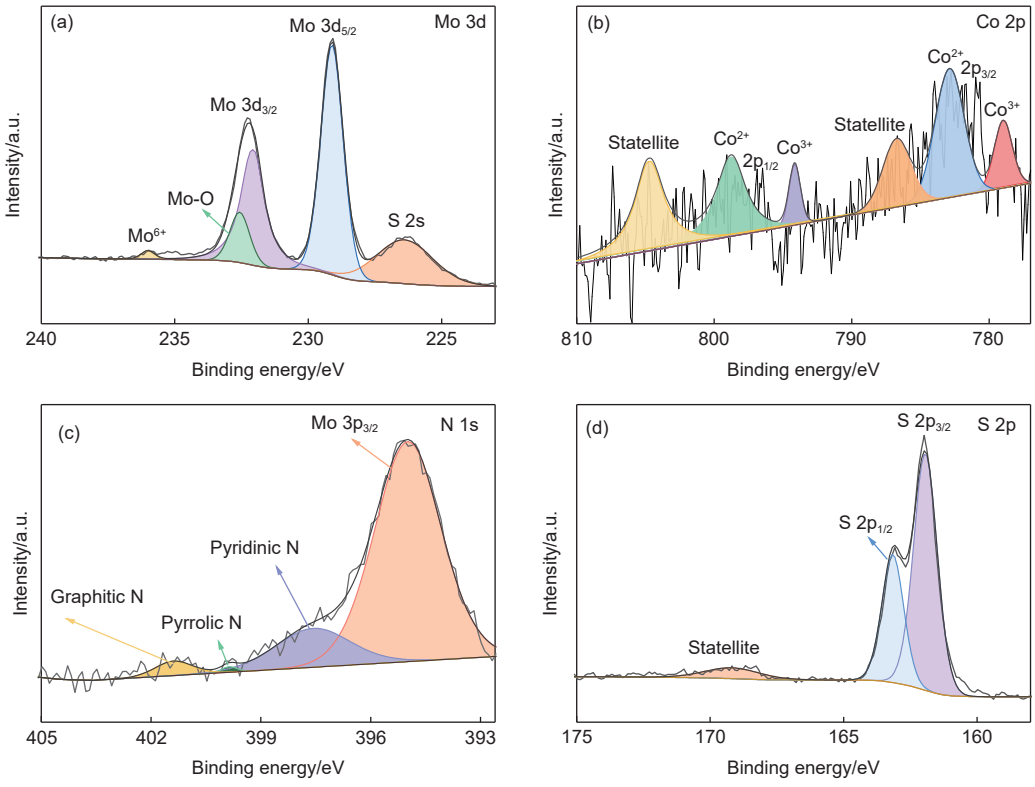

Fig. 2 XPS spectra of the Co_9S_8/MoS_2/C-700: (a) Mo 3d spectra, (b) Co 2p spectra, (c) N 1s spectra and (d) S 2p spectra

sample is probably due to exposure of the samples to air[42]. The valence and bonds of all elements in Co_9S_8/MoS_2/C-700 composite have been verified by the XPS analysis.

3.2 Electrochemical performance

The electrode materials were assembled into SIBs to test its cycle stability and rate performance. In the first charge and discharge process (Fig. 3a), Co_9S_8/MoS_2/C-700 electrode displays the specific capacities of approximately 732 and 887 mAh g^{-1}, higher than that of the Co_9S_8/MoS_2/C-600 (521 and 619 mAh g^{-1}) and the Co_9S_8/MoS_2/C-800 (521 and 383 mAh g^{-1}). Fig. 3b shows the first 5 CV cycles of the Co_9S_8/MoS_2/C-700 composite electrode. Some peaks can be observed in the first cathode curve. For each redox peak, the corresponding electrochemical process is distinguished, where the wide peak between 0.6 and 0.4 V is due to the formation of the solid electrolyte interface (SEI) layer, resulting in irreversible capacity loss and lower Coulombic efficiency (CE) in the first cycle. The peaks at 1.2 and 1.0 V correspond to the formation of Na_xMoS_2 by Na^+ embedded in MoS_2 interlayers and the multistep reduction of Co_9S_8 to metals Co and Na_2S. The spike near 0.1 V was attributed to the conversion of Na_xMoS_2 into metal Mo and Na_xS[43]. The last 4 cyclic cathode curves show nearly the same characteristics. The peaks of the multistep reduction of Co_9S_8 and Na^+ embedding in MoS_2 interlayer move to higher voltages of 1.5 and 0.85 V, indicating an active process in the first cycle. During the charging process, one main oxidation peak at 1.8 V is observed on the anodic curves, which is attributed to the decomposition of Na_2S into Na^+ and S. During the subsequent cycles, the oxidation peaks are repeatable, but the reduction peaks are not, implying irreversible reactions[44].

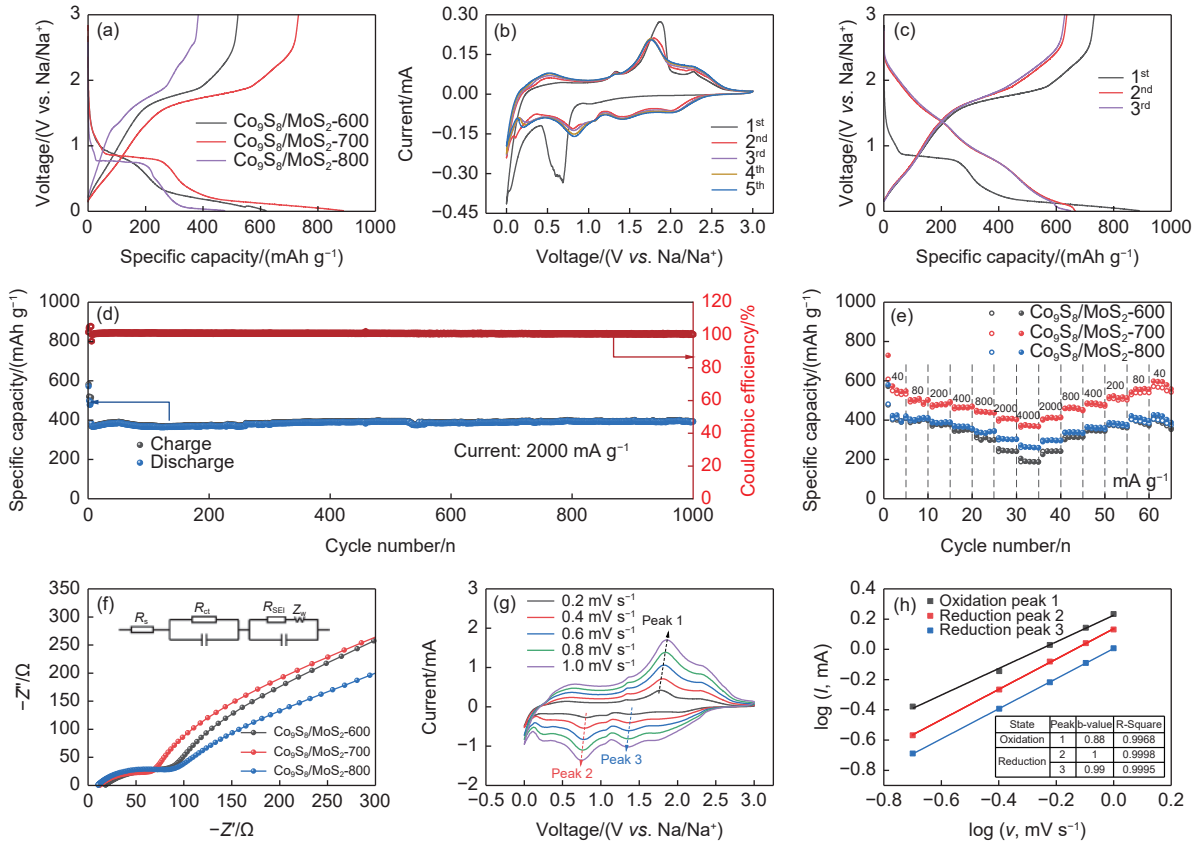

Fig. 3　Sodium storage performance of the electrode: (a) charge–discharge profiles at 40 mA g^{-1} and (b) CV curves at a voltage window of 0.01-3 V for the Co_9S_8/MoS_2/C–700 composite. (c) Cycle performance at 40 mA g^{-1}, (d) cycle performance at 2 000 mA g^{-1} and (e) rate capability at different current densities for the Co_9S_8/MoS_2/C-600 composite, Co_9S_8/MoS_2/C-700 and Co_9S_8/MoS_2/C-800 anodes. Note that the electrodes were first 5 cycles activated at 40 mA g^{-1} for a few cycles. (f) Nyquist plots of the Co_9S_8/MoS_2/C-600, Co_9S_8/MoS_2/C-700 and Co_9S_8/MoS_2/C-800 electrode materials. (g) CV curves at different scan rates and (h) the peak current plotted against scan rates at 3 specific redox peaks of Co_9S_8/MoS_2/C-700

Fig. 3c shows a comparison of the discharge-charge curves for the 1st, 2nd, and 3rd cycles of Co_9S_8/MoS_2/C-700 composite electrode at 40 mA g^{-1}. Two voltage plateaus could be observed at approximately 0.85 and 0.2. 0.01 V could be observed in the discharge curves of the Co_9S_8/MoS_2/C electrode, which coincide with the CV results[45]. The initial Coulombic efficiency is 82.5%. The capacity loss comes mainly from the formation of SEI film and some side reactions during the initial sodiation process, which leads to the low initial Coulombic efficiency[46]. The charge-discharge curves of the electrode material show no discrepancy in the subsequent cycles. At 800 mA g^{-1}, the results of the cyclic stability test are shown in Fig. S5. In the initial 5 cycles, a low current density of 40 mA g^{-1} is applied to generate a dense stable SEI film. After 100 cycles, the specific capacities of pure Co_9S_8 (Fig. S6), Co_9S_8/MoS_2/C-600 and Co_9S_8/MoS_2/C-800 are 191 mAh g^{-1}, 192 mAh g^{-1} and 309 mAh g^{-1}, respectively. The Co_9S_8/MoS_2/C-700 still shows the highest specific capacity of 535 mAh g^{-1}. The cycling performance of Co_9S_8/MoS_2/C-700 at a current density of 2 000 mA g^{-1} in the range of 0–3 V and the 1 000th cycle discharge capacity of 394.4 mAh g^{-1} is presented in Fig. 3d. The rate capabilities of the electrodes were evaluated at 40, 80, 200, 400, 800, 2 000 and 4 000 mA g^{-1}, as depicted in Fig. 3e. Five cycles were conducted for each current density. The reversible capacities of Co_9S_8/MoS_2/C reached 368 mAh g^{-1} at 4 000 mA g^{-1} with capacity retention rate of 68.9% compared to the capacity at 40 mA g^{-1}. Under the same conditions, the capacity retention was only 45.8% and 62.8% for the Co_9S_8/MoS_2/C-600 and Co_9S_8/MoS_2/C-800 anodes, respectively. When the current density returns from 4 000 to 40 mA g^{-1}, the discharge capacity of the Co_9S_8/MoS_2/C-700 can be fully recovered from 368 to 571 mAh g^{-1} and then stable at 543 mAh g^{-1} after some cycles, indicating that the sample Co_9S_8/MoS_2/C-700 composite has a high sustainability. In contrast, Co_9S_8/MoS_2/C-600 and Co_9S_8/MoS_2/C-800 electrodes show poor rate capability[47]. The performance of Co_9S_8/MoS_2/C anode is significantly better than that of Co- and Mo-based transition metal sulfide anodes previously reported, suggesting that Co_9S_8/MoS_2/C is a attractive candidate for SIB anode (Table S1).

To gain further insight into the sodium storage performance of the above material, electrochemical impedance spectroscopy (EIS) was employed at the open circuit potential. The corresponding resistance values were obtained by the simulation of testing data with the equivalent circuit model. As displayed in Fig. 3f, the charge transfer resistance (R_{ct}) of Co_9S_8/MoS_2/C-700 composite electrode is 71.2 Ω, which is smaller than those of Co_9S_8/MoS_2/C-600 (97.7 Ω) and Co_9S_8/MoS_2/C-800 (85.6 Ω). The smaller value indicates a faster electron transfer capacity[48]. The results imply that the electrochemical reaction rate and electrical conductivity of Co_9S_8/MoS_2/C-700 composite are superior to the other two electrodes[49].

CV tests (Fig. 3g) were carried out at different scanning speeds of 0.2-1.0 mV s^{-1} to further evaluate the kinetics of Co_9S_8/MoS_2/C-700 electrode materials for improved performance[50]. The CV curves for Co_9S_8/MoS_2/C-600 and Co_9S_8/MoS_2/C-800 electrodes have similar shapes as the scan rate increases, indicating a similar Na^+ storage mechanism (Fig. S7a,c)[51]. Furthermore, with increasing scan rates, the shape of the curves remain nearly the same, suggesting high rate capability. Different mechanisms account for different contributions to the total battery capacity, so the following formula is used to further understand the behaviours that affect electrochemical performance.

Hence, we introduce the formula[52]:

$$i = av^b \quad (1)$$

where i means the responsive current (mA), v represents the scan rate (mV s^{-1}), and a and b are constants. To facilitate the calculation, linear equation $\log i = b\log v + \log a$ of current and scan rate is obtained by taking logarithms of the 2 sides of equation (1).

The dominant charge-storage mechanism can be distinguished from the slope of the b-value. Specifically, when the b is 0.5, the battery system is mainly dominated by the ion intercalation process. While the value of b approaches 1, it expresses a characteristic

of the capacitive behaviour with fast kinetics[53]. By calculating peak current i and scanning rate v, a straight line for each redox peak was drawn and linear fitting was carried out. In Fig. 3h, the b values for the redox peaks of the Co_9S_8/MoS_2/C-700 electrode are calculated to be 0.88, 1.00 and 0.99, indicating that the Co_9S_8/MoS_2/C-700 electrode is dominated by the surface capacitive behavior. Furthermore, the Co_9S_8/MoS_2/C-700 electrode exhibits larger b values at all redox peaks compared to those of the Co_9S_8/MoS_2/C-600 and Co_9S_8/MoS_2/C-800 electrode (Fig. S7b,d), suggesting a faster reaction kinetics[54].

Furthermore, the contribution of surface capacitance to current responsiveness can be estimated using the formula $i = k_1v + k_2v^{1/2}$[55]. In this formula, k_1v and $k_2v^{1/2}$ represent the current of the pseudocapacitive behavior and the diffusive behavior, respectively. By calculating the values of k_1 and k_2, the ratio of the 2 capacity contribution behaviours at this point can be obtained[56]. For example, at 0.2 mV s^{-1}, the capacitance contribution percentage is about 94.47% of the total capacity, as shown in the shaded area in Fig. S8a. At other scan rates, the quantitative contributions of the two electrochemical behaviours are also plotted in Fig. S8b. The capacitive contribution increased from 94.47% to 97.32% when the scanning rate was 0.2-1.0 mV s^{-1}. With the increase of scan rate, the gradual increase in capacitance contribution rate may be due to its unique structural characteristics (the outer layer is a fluffy MoS_2 crossed nanosheet array), which promotes the rapid transfer of electrons or ions and affords the battery excellent rate capability and long-life stability[57–58].

3.3 Computational results

Density functional theory (DFT) calculations were performed to verify the effect of the constructed Co_9S_8/MoS_2 heterostructure on enhanced electrochemical performance. According to the DFT calculation, Co_9S_8(001) facets and single layer MoS_2 were chosen to build the heterointerface. The optimized crystal structures of bulk Co_9S_8, MoS_2, and the Co_9S_8(001)/MoS_2 heterostructure are shown in Fig. S9. The stability of Co_9S_8/MoS_2 heterojunction can be proved by the formation of interface adhesion, and the equation is as follows

$$E_F = E_{Co_9S_8(001)/MoS_2} - E_{Co_9S_8(001)} - E_{MoS_2} \quad (2)$$

where $E_{Co_9S_8(001)/MoS_2}$, $E_{Co_9S_8(001)}$ and E_{MoS_2} represent the total energy of the relaxed Co_9S_8(001)/MoS_2 heterojunction, Co_9S_8(001) slab and single layer MoS_2, respectively. The calculated interface formation energy was −210.59 eV for the entire model interface. The negative value energy indicated that the Co_9S_8(001)/MoS_2 composite could form a stable heterogeneous interface.

To investigate the interface performance of the Co_9S_8(001)/MoS_2 heterostructure, we calculated the band structure of the Co_9S_8(001) slab and MoS_2. The band structures are depicted in Fig. S10. Meanwhile, the electronic density of states (DOS) of bulk Co_9S_8, MoS_2 and Co_9S_8(001)/MoS_2 were also calculated for comparison. DOS curves in Fig. 4a-c and the band structures show that the bandgap value of pure MoS_2 is about 1.42 eV. The bandgap is similar to the results in Material Project (MoS_2 mp-2815: 1.46). When Co_9S_8 is introduced into MoS_2, the state density of Co_9S_8(001)/MoS_2 composite cross the Fermi level, which indicates that the electronic structure is reshaped at the interface of the heterogeneous structure and exhibits typical metallic properties and enhanced electronic conductivity.

The charge transfer and separation of the Co_9S_8(001)/MoS_2 heterojunction were studied by calculating the three-dimensional charge density difference of the heterojunction, and the results are shown in Fig. 4d. The violet and aquamarine areas indicate electron depletion and accumulation, respectively. The plane-integrated electron density difference along Z-direction shows the result of charge distribution in Fig. 4e. Positive values indicate electron accumulation, and negative values indicate electron depletion. The electronic properties of Co_9S_8(001)/MoS_2 heterojunction were calculated based on the constructed model, and the interface charge transfer path and formation mechanism of Co_9S_8(001)/MoS_2 heterojunction were further investigated. The electrostatic potentials of Co_9S_8(001) surface (Fig. S11a), single

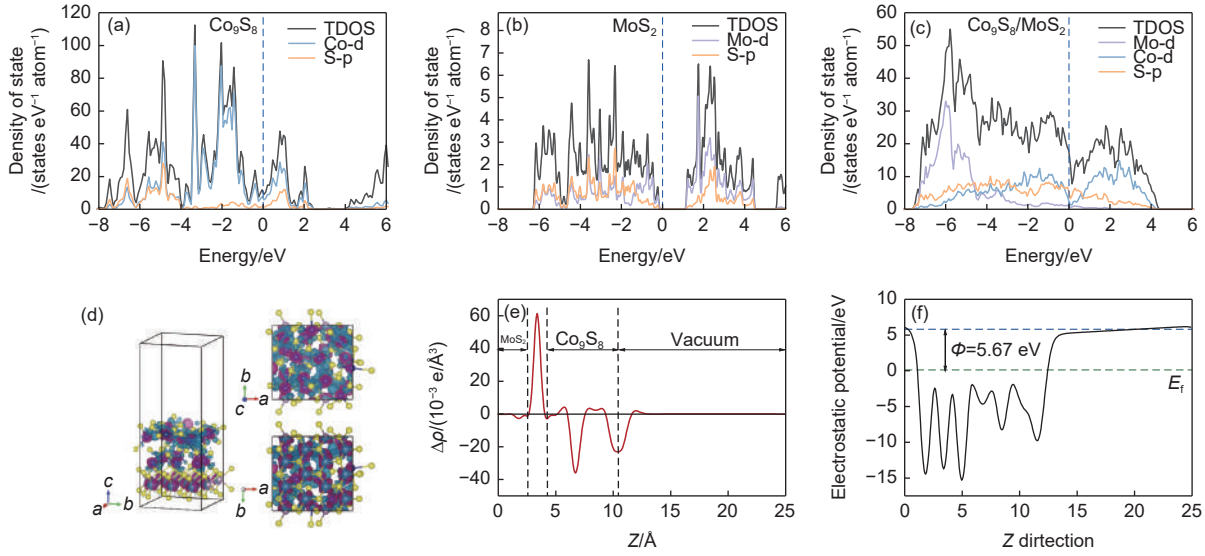

Fig. 4 (a) The calculated PDOS of Co and S atoms in Co_9S_8. (b) The calculated PDOS of Mo and S atoms. (c) Calculated TDOS of Co_9S_8/MoS_2 heterojunction and PDOS of Mo, Co and S. (d) The side view, top view and bottom view of the charge density difference (0.015 e·bohr^{-3}) for Co_9S_8/MoS_2. (e) Planar-averaged electron density difference $\Delta\rho(z)$ for Co_9S_8/MoS_2. The violet and aquamarine areas indicate electron depletion and accumulation regions, respectively. (f) Co_9S_8/MoS_2 heterojunction slab model. The green and blue dashed lines denote Fermi level and the vacuum energy level, respectively

layer MoS_2 (Fig. S11b) and $Co_9S_8(001)/MoS_2$ heterojunction (Fig. 4f) were calculated. According to the definition of work function, the work functions of $Co_9S_8(001)$, MoS_2 and $Co_9S_8(001)/MoS_2$ heterojunctions are 6.00, 5.55 and 5.67 eV, respectively[59]. When $Co_9S_8(001)$ contacts MoS_2, the work function of $Co_9S_8(001)$ is higher than that of MoS_2, causing the electrons to move from MoS_2 to $Co_9S_8(001)$ until the Fermi energy of the 2 structures was aligned. Hence, $Co_9S_8(001)$ accumulated a negative charge on the surface. Instead, the MoS_2 layer accumulates a positive charge. This result accords with the charge density difference and Band charge analysis.

4 Conclusion

In conclusion, a facile self-templated method was developed to prepare $Co_9S_8/MoS_2/C$ composite by simultaneous vulcanization and carbonization at 600 °C, 700 °C and 800 °C on Co-ZIF precursors. Due to the 3D structure of the synthesized $Co_9S_8/MoS_2/C$ material, the pulverization and volume expansion of the electrode material caused by the (de-)intercalation of sodium ions during charge and discharge could be relieved, and the stability of the structure was maintained. Benefiting from the excellent porous structure of $Co_9S_8/MoS_2/C$-700, the composite material has a relatively high reversible specific capacity when used in SIBs. At a current density of 4 000 mA g^{-1}, the material has a rate performance of 368 mAh g^{-1}. In addition, it is worth noting that when the current density is restored to 40 mA g^{-1} and the specific capacity is rapidly restored to 571 mAh g^{-1}, indicating that the material has good reversibility throughout the electrochemical reaction process. Furthermore, the DFT calculation shows that when Co_9S_8 is introduced into MoS_2, the state density of the $Co_9S_8(001)/MoS_2$ compound crosses the Fermi level, which indicates that the electronic structure is reshaped at the interface of the heterogeneous structure, thus $Co_9S_8(001)/MoS_2$ exhibits typical metal properties and enhanced electronic conductivity. The effect of heterojunction on electron/ion diffusion kinetics is proved. In summary, $Co_9S_8(001)/MoS_2$ heterojunction can effectively promote the electrochemical performance of MoS_2 as SIBs anode, hinting at promising application prospects. Going beyond the composites reported in this paper, we expect that the concept of MOF-derived nanoengineering design will provide a reference for the development of anode electrode material for the next generation of secondary battery systems.

Acknowledgements

This work was supported by the National Natural Science Foundation of China (52272194, 52204308), Liaoning Revitalization Talents Program (XLYC2007155) and the Fundamental Research Funds for the Central Universities (N2025018, N2025009) and China Postdoctoral Science Foundation (2022M710639).

References

[1] Mahmood N, Tang T, and Hou Y. Nanostructured anode materials for lithium ion batteries: Progress, challenge and perspective[J]. Advanced Energy Materials, 2016, 6(17): 1600374.

[2] Liu Z M, Wang J, Ding H B, et al. Carbon nanoscrolls for aluminum battery[J]. ACS Nano, 2018, 12(8): 8456-8466.

[3] Delmas C. Sodium and sodium-ion batteries: 50 years of research[J]. Advanced Energy Materials, 2018, 8 (17): 1703137.

[4] Liu Z M, Wang J, and Lu B A. Plum pudding model inspired $KVPO_4F$@3DC as high-voltage and hyperstable cathode for potassium ion batteries[J]. Science Bulletin, 2020, 65(15): 1242-1251.

[5] Liu Z M, Wang J, Jia X X, et al. Graphene armored with a crystal carbon shell for ultrahigh-performance potassium ion batteries and aluminum batteries[J]. ACS Nano, 2019, 13(9): 10631-10642.

[6] Ellis B L and Nazar L F. Sodium and sodium-ion energy storage batteries[J]. Current Opinion in Solid State & Materials Science, 2012, 16(4): 168-177.

[7] Balogun M S, Luo Y, Qiu W T, et al. A review of carbon materials and their composites with alloy metals for sodium ion battery anodes[J]. Carbon, 2016, 98: 162-178.

[8] Zhao C Y, Wang X, Kong J H, et al. Self-assembly-induced alternately stacked single-layer MoS_2 and N-doped graphene: A novel van der waals heterostructure for lithium-ion batteries[J]. ACS Applied Materials & Interfaces, 2016, 8(3): 2372-2379.

[9] Kong D Z, Cheng C W, Wang Y, et al. Fe_3O_4 quantum dot decorated MoS_2 nanosheet arrays on graphite paper as free-standing sodium-ion battery anodes[J]. Journal of Materials Chemistry A, 2017, 5(19): 9122-9131.

[10] Su D W, Dou S X, and Wang G X. Ultrathin MoS_2 nanosheets as anode materials for sodium-ion batteries with superior performance[J]. Advanced Energy Materials, 2015, 5(6), 1401205.

[11] Lao M M, Zhang Y, Luo W B, et al. Alloy-based anode materials toward advanced sodium-ion batteries [J]. Advanced Materials, 2017, 29(48): 1700622.

[12] Zhou L F, Gao X W, Du T, et al. Two-dimensional NbSSe as anode material for low-temperature sodium-ion batteries[J]. Chemical Engineering Journal, 2022, 435: 134838.

[13] Zhou F, Xin S, Liang H W, et al. Carbon nanofibers decorated with molybdenum disulfide nanosheets: synergistic lithium storage and Enhanced Electrochemical Performance[J]. Angewandte Chemie-International Edition, 2014, 53(43): 11552-11556.

[14] Yu X Y, Hu H, Wang Y W, et al. Ultrathin MoS_2 nanosheets supported on N-doped carbon nanoboxes with enhanced lithium storage and electrocatalytic properties[J]. Angewandte Chemie-International Edition, 2015, 54(25): 7395-7398.

[15] Zhao L, Yu X Q, Yu J Z, et al. Remarkably improved electrode performance of bulk MnS by forming a solid solution with FeS-understanding the Li storage mechanism[J]. Advanced Functional Materials, 2014, 24(35): 5557-5566.

[16] Chen G, Yan L T, Luo H M, et al. Nanoscale engineering of heterostructured anode materials for boosting lithium-ion storage[J]. Advanced Materials, 2016, 28(35): 7580-7602.

[17] Cao L, Liang X H, Ou X, et al. Heterointerface engineering of hierarchical Bi_2S_3/MoS_2 with self-generated rich phase boundaries for superior sodium storage performance[J]. Advanced Functional Materials, 2020, 30(16): 1910732.

[18] Ni J F, Sun M L, Li L. Highly efficient sodium storage in iron oxide nanotube arrays enabled by built-in electric field[J]. Advanced Materials, 2019, 31(41): 1902603.

[19] Luo W, Li F, Li Q D, et al. Heterostructured Bi_2S_3-Bi_2O_3 nanosheets with a built-in electric field for improved sodium storage[J]. ACS Applied Materials & Interfaces, 2018, 10(8): 7201-7207.

[20] Zheng Y, Zhou T F, Zhang C F, et al. Boosted charge transfer in SnS/SnO_2 heterostructures: Toward high rate capability for sodium-ion batteries[J]. Angewandte Chemie-International Edition, 2016, 55(10): 3408-3413.

[21] Wang Y Z, Xie W Y, Li D Z, et al. One-pot synthesis of hierarchical $Co_{1-X}S$/NC@MoS_2/C hollow nanofibers based on one-dimensional metal coordination polymers for enhanced lithium and sodium-ion storage[J]. Science Bulletin, 2020, 65(17): 1460-1469.

[22] Chen F Z, Shi D, Yang M Z, et al. Novel designed MnS-MoS_2 heterostructure for fast and stable Li/Na storage: Insights into the advanced mechanism attributed to phase engineering[J]. Advanced Functional Materials, 2021, 31(6), 2007132.

[23] Furukawa H, Cordova K E, O'Keeffe M, et al. The chemistry and applications of metal-organic frameworks[J]. Science, 2013, 341(6149): 1230444.

[24] Wales D J, Grand J, Ting V P, et al. Gas sensing using porous materials for automotive applications[J]. Chemical Society Reviews, 2015, 44(13): 4290-4321.

[25] Chughtai A H, Ahmad N, Younus H A, et al. Metal-organic frameworks: Versatile heterogeneous catalysts for efficient catalytic organic transformations[J]. Chemical Society Reviews, 2015, 44(19): 6804-6849.

[26] Xu X, Cao R, Jeong S, et al. Spindle-like mesoporous alpha-Fe_2O_3 anode material prepared from MOF template for high-rate Lithium batteries[J]. Nano Letters, 2012, 12(9): 4988-4991.

[27] Cao X H, Zheng B, Rui X H, et al. Metal oxide-coated three-dimensional graphene prepared by the use of metal-organic frameworks as precursors[J]. Angewandte Chemie-International Edition, 2014, 53(5): 1404-1409.

[28] Cao X H, Zheng B, Shi W H, et al. Reduced graphene oxide-wrapped MoO_3 composites prepared by using metal-organic frameworks as precursor for all-solid-state flexible supercapacitors[J]. Advanced Materials, 2015, 27(32): 4695-4701.

[29] Zhao M T, Wang Y X, Ma Q L, et al. Ultrathin 2D metal-organic framework nanosheets[J]. Advanced Materials, 2015, 27(45): 7372-7378.

[30] Pan Y, Sun K, Liu S, et al. Core-shell ZIF-8@ZIF-67-derived CoP nanoparticle-embedded N-doped carbon nanotube hollow polyhedron for efficient overall water splitting[J]. J Am Chem Soc, 2018, 140(7): 2610-2618.

[31] Kresse G and Hafner J. Ab initio molecular dynamics for liquid metals[J]. Phys Rev B Condens Matter, 1993, 47(1): 558-561.

[32] Kresse G and Hafner J. Ab initio molecular-dynamics simulation of the liquid-metal-amorphous-semiconductor transition in germanium[J]. Phys Rev B Condens Matter, 1994, 49(20): 14251-14269.

[33] Zhou L F, Gao X W, Du T, et al. New phosphate $Zn_2Fe(Po_4)_2$ cathode material for nonaqueous zinc ion batteries with long life span[J]. ACS Applied Materials & Interfaces, 2022, 14(7): 8888-8895.

[34] Lai L F, Huang G M, Wang X F, et al. Solvothermal syntheses of hollow carbon microspheres modified with $-NH_2$ and -OH groups in one-step process[J]. Carbon, 2010, 48(11): 3145-3156.

[35] Shao J, Gao T, Qu Q T, et al. Ultrafast Li-storage of MoS_2 nanosheets grown on metal-organic framework-derived microporous nitrogen-doped carbon dodecahedrons[J]. Journal of Power Sources, 2016, 324: 1-7.

[36] Wu A P, Tian C G, Yan H J, et al. Hierarchical MoS_2@MoP core-shell heterojunction electrocatalysts for efficient hydrogen evolution reaction over a broad ph range[J]. Nanoscale, 2016, 8(21): 11052-11059.

[37] Li Y P, Liu J D, Chen C, et al. Preparation of NiCoP hollow quasi-polyhedra and their electrocatalytic properties for hydrogen evolution in alkaline solution[J]. ACS Applied Materials & Interfaces, 2017, 9(7): 5982-5991.

[38] Yu Z Y, Duan Y, Gao M R, et al. A one-dimensional porous carbon-supported Ni/Mo_2C dual catalyst for efficient water splitting[J]. Chemical Science, 2017, 8(2): 968-973.

[39] Zhu Z, Yang Y, Guan Y, et al. Construction of a cobalt-embedded nitrogen-doped carbon material with the desired porosity derived from the confined growth of MOFs within graphene aerogels as a superior catalyst towards HER and ORR[J]. Journal of Materials Chemistry A, 2016, 4(40): 15536-15545.

[40] Wang J J, Luo C, Gao T, et al. An advanced MoS_2/carbon anode for high-performance sodium-ion batteries[J]. Small, 2015, 11(4): 473-481.

[41] Geng H, Yang J, Dai Z, et al. Co_9S_8/MoS_2 yolk-shell spheres for advanced Li/Na storage[J]. Small, 2017, 13(14), 1603490.

[42] Li D H, Sun Y Y, Chen S, et al. Highly porous FeS/carbon fibers derived from Fe-carrageenan biomass: High-capacity and durable anodes for sodium-ion batteries[J]. ACS Applied Materials & Interfaces, 2018, 10(20): 17175-17182.

[43] Shi Z T, Kang W P, Xu J, et al. Hierarchical nanotubes assembled from MoS_2-carbon monolayer sandwiched superstructure nanosheets for high-performance sodium ion batteries[J]. Nano Energy, 2016, 22: 27-37.

[44] Zhang Z, Gan Y Q, Lai Y Q, et al. Cobalt sulfides/dodecahedral porous carbon as anode materials for Na-ion batteries[J]. RSC Advances, 2015, 5(125): 103410-103413.

[45] Wang P, Gou W, Jiang T, et al. An interlayer spacing design approach for efficient sodium ion storage in N-doped MoS_2[J]. Nanoscale Horiz, 2023, 8: 473–482.

[46] Li H, Su Y, Sun W W, et al. Carbon nanotubes rooted in porous ternary metal sulfide@N/S-doped carbon dodecahedron: Bimetal-organic-frameworks derivation and electrochemical application for high-capacity and long-life lithium-ion batteries[J]. Advanced Functional Materials, 2016, 26(45): 8345-8353.

[47] Tang L B, Li P Y, Cui R D, et al. Adjusting crystal orientation to promote sodium-ion transport in V_5S_8@graphene anode materials for high-performance sodium-ion batteries[J]. Small Methods, 2023, 7(2): 2201387.

[48] Zhou W J, Lu J, Zhou K, et al. $CoSe_2$ nanoparticles embedded defective carbon nanotubes derived from MOFs as efficient electrocatalyst for hydrogen evolution reaction[J]. Nano Energy, 2016, 28: 143-150.

[49] Chen Q, Sun S, Zhai T, et al. Yolk-shell NiS_2 nanoparticle-embedded carbon fibers for flexible fiber-shaped sodium battery[J]. Advanced Energy Materials, 2018, 8(19), 1800054.

[50] Zhao D C, Zhang Z, Ren J H, et al. Fe_2VO_4 nanoparticles on rGO as anode material for high-rate and durable lithium and sodium ion batteries[J]. Chemical Engineering Journal, 2023, 451: 138882.

[51] Li S K, Zhang S S, Liu Z J, et al. Self-assembled monodisperse $FeSe_2$ microflowers as an advanced anode material for sodium ion batteries[J]. Sustainable Energy & Fuels, 2022, 6(10): 2498-2502.

[52] Li H Y, Cheng Z, Zhang Q, et al. Bacterial-derived, compressible, and hierarchical porous carbon for high-performance potassium-ion batteries[J]. Nano Letters, 2018, 18(11): 7407-7413.

[53] Fang Y J, Luan D Y, Chen Y, et al. Rationally designed three-layered Cu_2S@carbon@MoS_2 hierarchical nanoboxes for efficient sodium storage[J]. Angewandte Chemie-International Edition, 2020, 59(18): 7178-7183.

[54] Xu X, Zhao R S, Ai W, et al. Controllable design of MoS_2 nanosheets anchored on nitrogen-doped graphene: Toward fast sodium storage by tunable pseudocapacitance[J]. Advanced Materials, 2018, 30(27): 1800658.

[55] Chao D L, Zhu C R, Yang P H, et al. Array of nanosheets render ultrafast and high-capacity Na-ion storage by tunable pseudocapacitance[J]. Nature Communications, 2016, 7: 12122.

[56] Park M, Zhang X C, Chung M D, et al. A review of conduction phenomena in Li-ion batteries[J]. Journal of Power Sources, 2010, 195(24): 7904-7929.

[57] Ren X C, Zhao Y X, Li Q W, et al. A novel multielement nanocomposite with ultrahigh rate capacity and durable

performance for sodium-ion battery anodes[J]. Journal of Materials Chemistry A, 2020, 8(23): 11598-11606.

[58] Zhang X L, Huang L W, Zeng P, et al. Hierarchical MoS_2 anchored on core-shell Si@C with increased active-sites and charge transfer for superior cycling and rate capability in lithium-ion batteries[J]. Chemical Engineering Journal, 2019, 357: 625-632.

[59] Xia H, Yuan P, Zan L, et al. Evolution of stabilized 1T-MoS_2 by atomic-interface engineering of 2H-MoS_2/Fe-N_x towards enhanced sodium ion storage[J]. Angew Chem Int Ed Engl, 2023, 62(14): e2022182.